



Superior supercapacitive performance of hollow activated carbon nanomesh with hierarchical structure derived from poplar catkins

Xiao-Li Su ^a, Ming-Yu Cheng ^a, Lin Fu ^a, Jing-He Yang ^{b, **}, Xiu-Cheng Zheng ^{a, c, *}, Xin-Xin Guan ^{a, c}

^a College of Chemistry and Molecular Engineering, Zhengzhou University, Zhengzhou 450001, China

^b School of Chemical Engineering and Energy, Zhengzhou University, Zhengzhou 450001, China

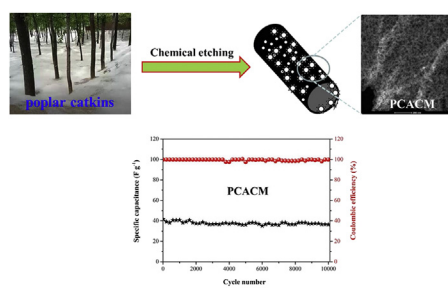
^c Key Laboratory of Advanced Energy Materials Chemistry (Ministry of Education), Nankai University, Tianjin 300071, China



HIGHLIGHTS

- Hollow active carbon nanomesh (PCACM) is derived from biowaste-poplar catkins.
- Hierarchical porous structure is constructed in PCACM architecture.
- PCACM achieves excellent supercapacitive performances.

GRAPHICAL ABSTRACT



ARTICLE INFO

Article history:

Received 5 April 2017

Received in revised form

18 June 2017

Accepted 4 July 2017

Available online 11 July 2017

Keywords:

Poplar catkins

Activated carbon nanomesh

Hierarchical porous structure

Electrochemical behaviors

Supercapacitors

ABSTRACT

The hollow activated carbon nanomesh (PCACM) with a hierarchical porous structure is derived from biowaste-poplar catkins by in-situ calcination etching with $\text{Ni}(\text{NO}_3)_2 \cdot 6\text{H}_2\text{O}$ and KOH in N_2 flow combined with an acid dissolution technique. This procedure not only inherits the natural tube morphology of poplar catkins, but also generates a fascinating nanomesh structure on the walls. PCACM possesses a large specific surface area ($S_{\text{BET}} = 1893.0 \text{ m}^2 \text{ g}^{-1}$) and high total pore volume ($V_p = 1.495 \text{ cm}^3 \text{ g}^{-1}$), and displays an exciting meso-macroporous structure with a concentrated pore size distribution of 4.53 nm. The specific capacitance of PCACM is as high as 314.6 F g^{-1} at 1.0 A g^{-1} when used as the electrode materials for supercapacitor. Furthermore, the symmetric supercapacitor of PCACM with $1.0 \text{ M Na}_2\text{SO}_4$ solution as the electrolyte displays a high energy density of 20.86 Wh kg^{-1} at a power density of 180.13 W kg^{-1} within a wide voltage rage of 0–1.8 V, which is comparable or even obviously higher than those of other biomass derived carbon reported. It is noteworthy that PCACM also exhibits superior cycling stability and coulombic efficiency. The excellent electrochemical behaviors enable PCACM to be a promising electrode material for supercapacitors.

© 2017 Elsevier B.V. All rights reserved.

1. Introduction

With the fast-growing energy demand in consumer electronics, electric vehicles, pulsing techniques as well as industrial power and energy management, great efforts have been made to exploit

* Corresponding author. College of Chemistry and Molecular Engineering, Zhengzhou University, Zhengzhou 450001, China.

** Corresponding author.

E-mail addresses: jhyang@zzu.edu.cn (J.-H. Yang), [\(X.-C. Zheng\)](mailto:zhxch@zzu.edu.cn).

various energy-related devices and to improve the efficiency of conversion and storage. Among the various energy storage devices, supercapacitors are considered as one of the potential energy storage systems due to their outstanding advantages including high power density, long cycle life, rapid charging discharging rate, simple principles and fast dynamics of charge propagation [1–3]. Depending on the energy storage mechanism, there are two types of supercapacitors: 1) The most commonly known ones are originally called electrical double layer capacitors (EDLC), which store and release energy based on electrostatic charge diffusion and accumulation in the double layer formed at the surface of inert electrodes; and 2) The other category of capacitor materials are the ones which store energy through reversible surface Faradaic redox reactions at the electrode/electrolyte interface [3,4]. It is known that the active electrode material is one of the most important factors to affect the electrochemical performance of supercapacitor. So far, various materials have been used as supercapacitor electrode materials, such as metal or metal alloys [5–7], polymers [8], metal oxides [9–16], metal sulfides [17,18], carbon based materials [19–39], and their composites [40–45] reported recently. Among these materials, carbon based ones exhibit highly stable reversible electrical energy storage capacity and high power density in EDLC ascribed the high specific surface area, high conductivity, suitable pore size distribution, and chemical stability.

As for carbon based materials, biomass is an environmentally friendly and renewable resource with abundant availability to serve as a cost-effective carbon precursor. Till now, various natural biomass materials, such as cellulose [29], pomelo peel [31], cotton [21,46], kenaf [47], bamboo shells [48], seed shells [49], and poplar catkins [50–52] have been used to prepare porous carbon. This not only greatly reduces the cost, but also inherits both the structural flexibility and chemical diversity of the natural resources. Even so, the specific surface area of biomass carbon materials is much lower than that of the others owing to the deficiency of micropores and small-diameter mesopores. Therefore, some chemical activation strategies have been used to adjust their textural structures [53–55]. The resulting porous structures could effectively promote the contact between the electrolytes and electrode material, and shorten the diffusion pathway of ions through the porous sheets, resulting in an excellent specific capacitance and a low capacitance loss. However, single chemical activation is not easy to control the geometry and size of the pores. In addition, the pore numbers are also limited. Hence, it is urgent to form a hierarchical structure with abundant meso-macropores, which could provide a high density of ion diffusion channels, facilitate charge storage and transport at high rates for high-performance energy storage devices.

In 2014, Wei [52] prepared carbon microtubes from poplar catkins by chemical activation with $ZnCl_2$, which yield a specific capacitance of 206 F g^{-1} and an energy density of 7.5 W h kg^{-1} when used as electrode material for supercapacitor. In this work, the hollow activated carbon nanomesh (PCACM) is derived from poplar catkins using a two-steps chemical activation procedure for the first time. The inherited tube morphology of poplar catkins and the generated abundant pores construct an admirably hierarchical structure in PCACM, which enhances the electrochemical stability and ion transport network, and improves the electrochemical behaviors. Eventually, as a supercapacitor electrode, PCACM exhibits much more excellent electrochemical performance than carbon produced by carbonizing poplar catkins without etching (PCC) and the ones etched only with KOH (PCAC) or $Ni(NO_3)_2 \cdot 6H_2O$ (PCAC[#]). Furthermore, its specific energy density is comparable or even obviously higher than those of biomass derived carbon reported. This enables PCACM to be a promising electrode material for high-performance supercapacitors.

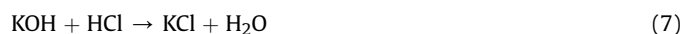
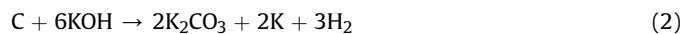
2. Experiments

2.1. Preparation of the samples

The pretreatment of poplar catkins which were collected from Zhengzhou city, P. R. China in April and May, was as follows: Firstly, a certain amount of poplar catkins were dispersed into absolute ethanol and stirred violently for about 3 h. Then, they were washed with DI water, and dealt with HNO_3 solution (1.0 mol L^{-1}) for 12 h to remove the seeds and impurities. Finally, the solid was filtered, washed with DI water and dried at 80°C overnight.

Fig. 1 shows the schematic illustration for the preparation of hollow carbon nanomesh from poplar catkins (PCACM). Firstly, poplar catkins were calcined and in-situ etched with KOH and $Ni(NO_3)_2$ in nitrogen atmosphere. Some pores would be produced due to the release of the gases (NO_2 , H_2 , CO_2 , and CO) produced in the reactions shown in Eqs. (1)–(5). Then, the resulting K and NiO reacted with hydrochloric acid shown in Eqs. (6)–(8) and left the nanomesh structure.

In brief, 2 g of dried poplar catkins was immersed with 10 wt% $Ni(NO_3)_2 \cdot 6H_2O$ ethanol solution at room temperature and followed by evaporating at 30°C in an air oven. After such process was repeated three times, the obtained solid was calcined at 600°C for 4 h with a ramp rate of 2°C min^{-1} under nitrogen atmosphere in a tubular furnace. The products were immersed with KOH solution (2.0 mol L^{-1}) with the mass ratio of 4: 1 (KOH: the resulting solids) and dried at 80°C . Then, it was activated at 800°C for 1 h with a ramp rate of 3°C min^{-1} under nitrogen atmosphere in a tubular furnace. The products were dispersed into HCl solution (1.0 mol L^{-1}) to consume K, NiO, and the residual KOH, washed with DI water and dried at 110°C .



For comparison, the dried poplar catkins were carbonized at 600°C for 4 h with a ramp rate of 2°C min^{-1} under nitrogen atmosphere and the resulting material was denoted as PCC. Furthermore, PCC was only activated with KOH, which was similar to that for PCACM without the immersion process of $Ni(NO_3)_2 \cdot 6H_2O$. The obtained material was denoted as PCAC. In addition, the dried poplar catkins was immersed with $Ni(NO_3)_2 \cdot 6H_2O$ ethanol solution at room temperature, evaporated at 30°C , calcined at 600°C , treated with HCl solution, washed with DI water, and dried at 110°C . This was same to that for PCACM without the immersion process of KOH and the further calcination at 800°C . The obtained material was denoted as PCAC[#].

2.2. Characterization

The textural parameters of the samples were obtained from nitrogen adsorption-desorption isotherms at -196°C using a

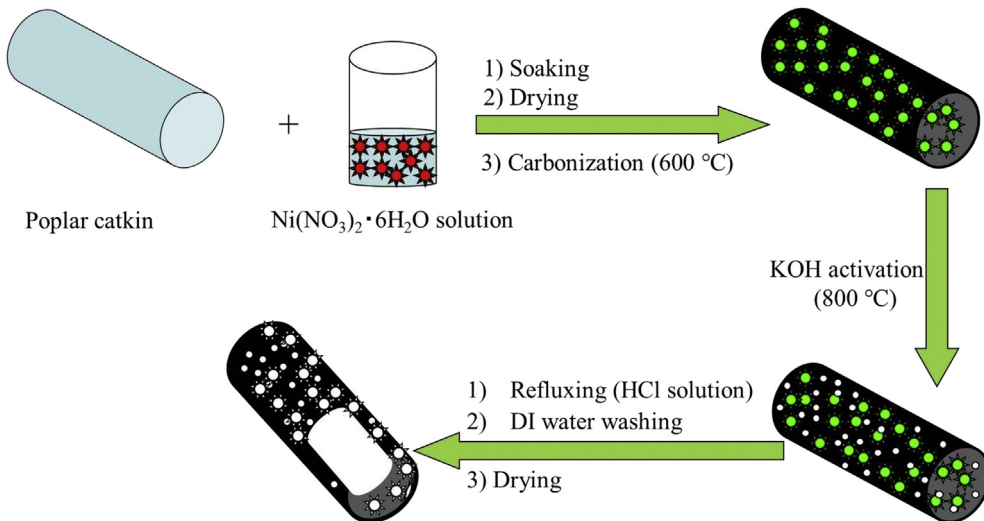


Fig. 1. Schematic illustration for the preparation of PCACM.

Micromeritics ASAP 2420-4 MP automated surface area and pore size analyzer. The specific surface area was calculated from the nitrogen adsorption isotherms by the Brunauer-Emmett-Teller (BET) method. The pore size distributions were measured from the adsorption branches by using the Barrett-Joyner-Halenda (BJH) method. The microstructures were examined using a Zeiss Ultra 55 scanning electron microscope (SEM) and a FEI Talos F200S transmission electron microscope (TEM). The phase structures were characterized by X-ray diffraction (XRD) on a Panalytical X'pertPro diffractometer operated at 40 kV and 40 mA using Cu K α radiation ($\lambda = 0.1546$ nm). Surface chemistry was studied by X-ray photoelectron spectroscopy (XPS) using an RBD upgraded PHI-5000C ESCA system (Perkin Elmer) and the binding energies were calibrated using the carbon (C1s = 284.6 eV). Raman spectra were recorded on a Renishaw RM-1000 spectrometer.

2.3. Electrochemical measurements

A three-electrode cell was used to evaluate the capacitive performance of the as-prepared materials on a CHI 660E electrochemical workstation (Shanghai ChenHua Instruments Co., China) in 6.0 M KOH aqueous electrolyte solution at room temperature. A platinum filament served as the counter electrode and an Ag/AgCl electrode acted as the reference electrode. The working electrode ($1.0 \times 1.0 \text{ cm}^2$) was consisted of 80 wt% the resulting material, 10 wt % acetylene black, and 10 wt% polytetrafluoroethylene binder and the mass loading of active materials on the working electrode is about 2–3 mg. The capacitive performance of samples was studied by using cyclic voltammetry (CV), galvanostatic charge-discharge (GCD) and electrochemical impedance spectroscopy (EIS) techniques. The CV curves were performed at different scan rates varying from 5 to 100 mV s⁻¹ at potentials between 0 and 1.0 V. Impedance spectroscopies were measured in the range of from 100 kHz to 10 mHz. The specific capacitance (C_m , F g⁻¹) of the resulting supercapacitors was calculated from the charge-discharge profiles by using Eq. (9) [56].

$$C_m = \frac{I_d \times \Delta t}{\Delta V \times m} \quad (9)$$

where I_d (mA) was the constant discharge current, Δt (s) was the discharge time, and ΔV (V) was the potential discharge voltage range. m (mg) was the mass of active materials in the working electrode.

The electrochemical behaviors of PCACM electrode were further investigated in a symmetric two-electrode supercapacitor device, which was fabricated by separating two electrodes with exactly the same mass soaked with 1.0 M Na₂SO₄ aqueous solution and the model battery jar were used as current collector. The CV tests of symmetric cell were operated in different voltage windows at 50 mV s⁻¹ and performed in the voltage range of 0–1.8 V by varying the scan rate from 5 to 100 mV s⁻¹. EIS was performed in a frequency range of 10 mHz–100 kHz at the open circuit voltage with alternate current amplitude of 5 mV. The specific capacitance of the two-electrode symmetrical supercapacitor cell (C_{cell} , F g⁻¹) was calculated from the GCD values by using Eq. (10).

$$C_{cell} = \frac{I \times t}{V \times m} \quad (10)$$

where I (A) is the discharge current, t (s) is the discharge time, m (g) is the total mass of anode and cathode materials and V (V) is the potential change in discharge. The specific energy density (E , Wh kg⁻¹) and specific power density (P , W kg⁻¹) of the symmetrical supercapacitor systems were calculated by using Eqs. (11) and (12), respectively.

$$E = \frac{1}{2} C_{cell} \times V^2 \quad (11)$$

$$P = \frac{E}{t} \quad (12)$$

Where V (V) is the cell-operation potential and t (h) is the discharge time.

3. Results and discussion

3.1. Characterization

Fig. 2 depicts the SEM images of PCC, PCAC, and PCACM. PCC shown in **Fig. 2a** and b exhibits a micro-tube morphology with a rough surface. As shown in **Fig. 2c** and e, reveal that PCAC and PCACM maintain the hollow structure of PCC. Meanwhile, the wall surfaces of PCAC and PCACM, especially in the case of PCACM, become much smoother than that of PCC due to the chemical etching of KOH and Ni(NO₃)₂·6H₂O. On the other hand, unlike the unbroken tube wall surface of PCC shown in **Fig. 2b**, it is observed

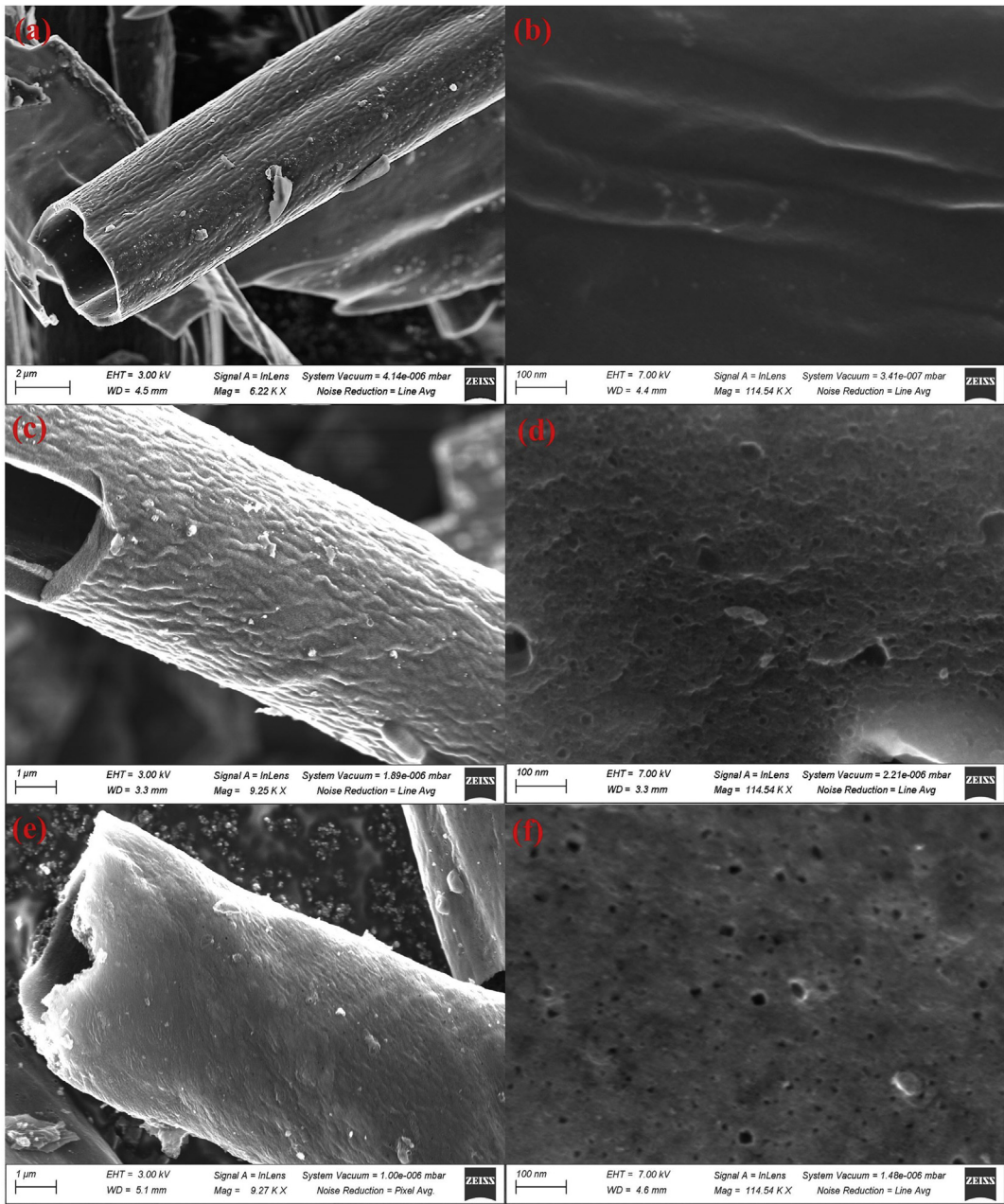


Fig. 2. SEM images of PCC (a, b), PCAC (c, d) and PCACM (e, f).

from Fig. 2d that some nano-pores appear in the surface of PCAC ascribed to the releasing of the gases produced in Eqs. (2)–(6) and the removal of K and residual KOH (Eqs. (6) and (7)). It is exciting that a nanomesh structure forms on the wall surface of PCACM ascribed to Eqs. (1)–(8) as discussed above. The SEM images under various magnifications shown in Fig. S1 (Electronic Supplementary Material, ESM) clearly confirm the micro-tube morphology and the nanomesh structure on the tube wall.

TEM analysis is further applied to confirm the microstructures of PCC, PCAC, and PCACM. The images shown in Fig. 3a and b presents the PCC are three-dimensional porous network structure with micrometer-level pores originated from its micro-tube morphology. Compared with PCC, the tube wall of PCAC and PCACM is thinner due to the surface was activated and etched by KOH (Fig. 3c–f). Meanwhile, it is noteworthy that a large number of

pores can be easily observed in their surfaces and much more abundant mesopores exist in than PCAC. The nanomesh structure on the wall of PCACM also could be clearly found in the scanning-transmission electron microscope (STEM) images shown in Fig. 4. Generally, the porous structure can offer conducted networks for fast electrons transfer and these pores can be helpful for the diffusion of electrolyte ions into the inner micro-mesopores, which is expected to improve the electrochemical performances of the electrode materials for supercapacitors.

The XRD patterns of the PCC, PCAC, and PCACM are shown in Fig. 5a. As shown in Fig. 5a, two broad peaks appear at around 23.4° and 43.9° in the pattern of PCC, which correspond to the diffractions of (002) and (100) planes of graphite lattice, respectively [56]. Although PCAC and PCACM also exhibit these typical planes, the peak intensity becomes weak even the (100) one disappears in the

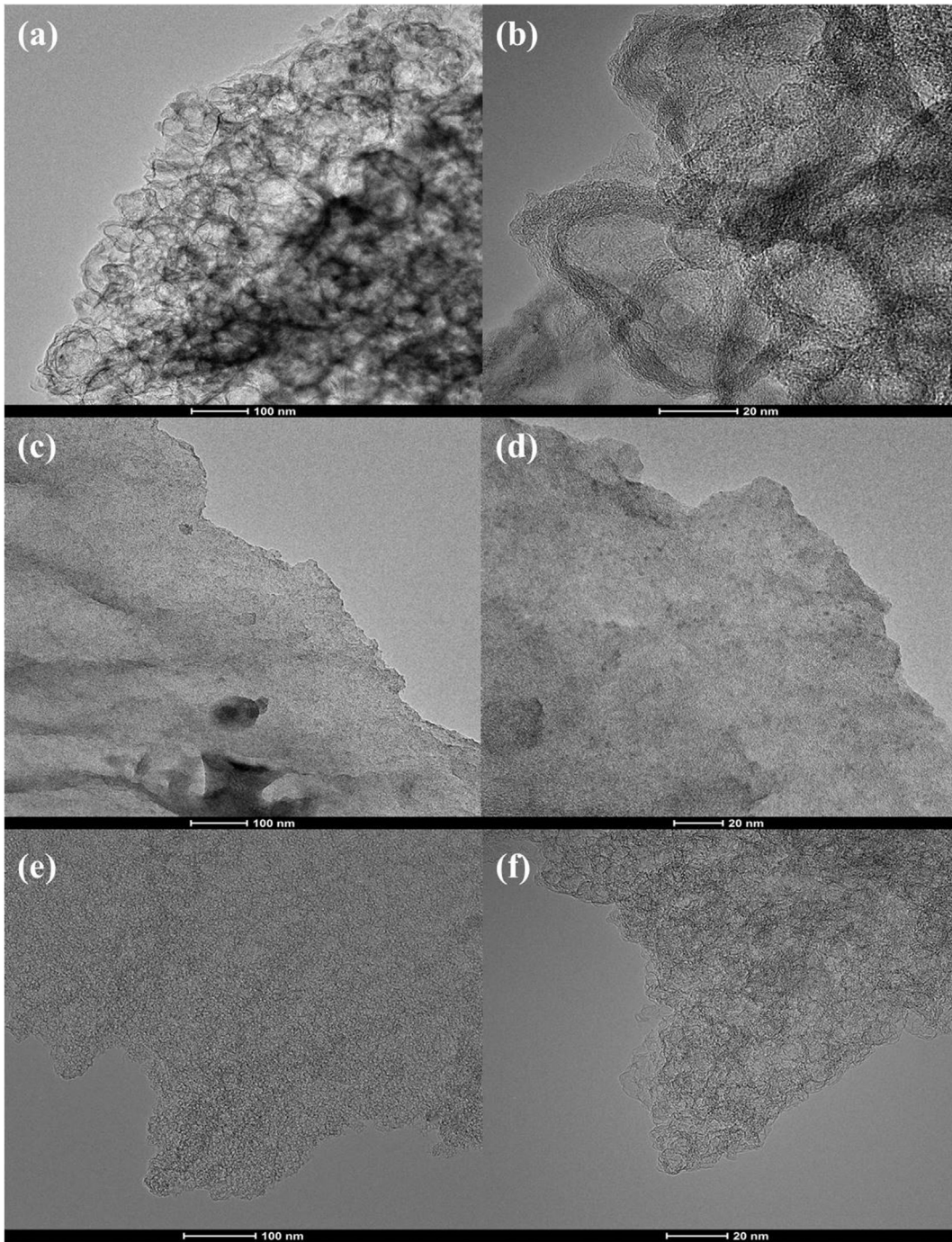


Fig. 3. TEM images of PCC (a, b), PCAC (c, d), and PCACM (e, f).

pattern of PCACM. Meanwhile, the (002) plane shifts slightly to the high angle. This suggests the existence of randomly stacked carbon because of the vacancy defects/nanomesh structure in PCACM, which is in agreement with the aforementioned electron microscope observations.

Raman spectra for the resulting materials shown in Fig. 5b display two prominent peaks at ca. 1329 cm^{-1} (D band) and 1587 cm^{-1} (G band), suggesting the crystallography and structure of the carbon materials. The D band is considered as a breathing mode of k-point phonons with A_{1g} symmetry caused by the local defects and the G band is derived from the E_{2g} phonon of C sp^2 atoms in the in-plane vibration of the graphitic structure [57].

Moreover, the intensity ratio of D band to G band (I_D/I_G) of PCC, PCAC, and PCACM are 0.99, 1.19, and 1.25, respectively, implying that the PCACM has more disordered and defective carbon than PCAC and PCC ascribed to its unique structure.

Nitrogen adsorption-desorption isotherms of PCC, PCAC, PCAC[#], and PCACM shown in Fig. 5c reveal that both PCC and PCAC have an increased steep at a low relative pressure range ($P/P_0 < 0.03$) and a flat plateau in the high pressure scope, implying that they are predominantly microporous under the analytic conditions. As for PCC, the pores are produced from the pyrolysis of poplar catkins and the evaporation of H_2O , CO_2 and NO_x during the carbonization process. While the additional pores in PCAC is produced by the

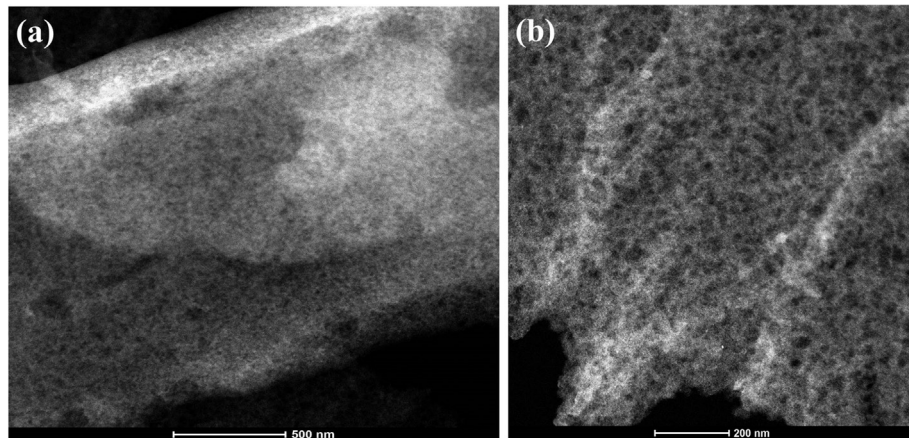
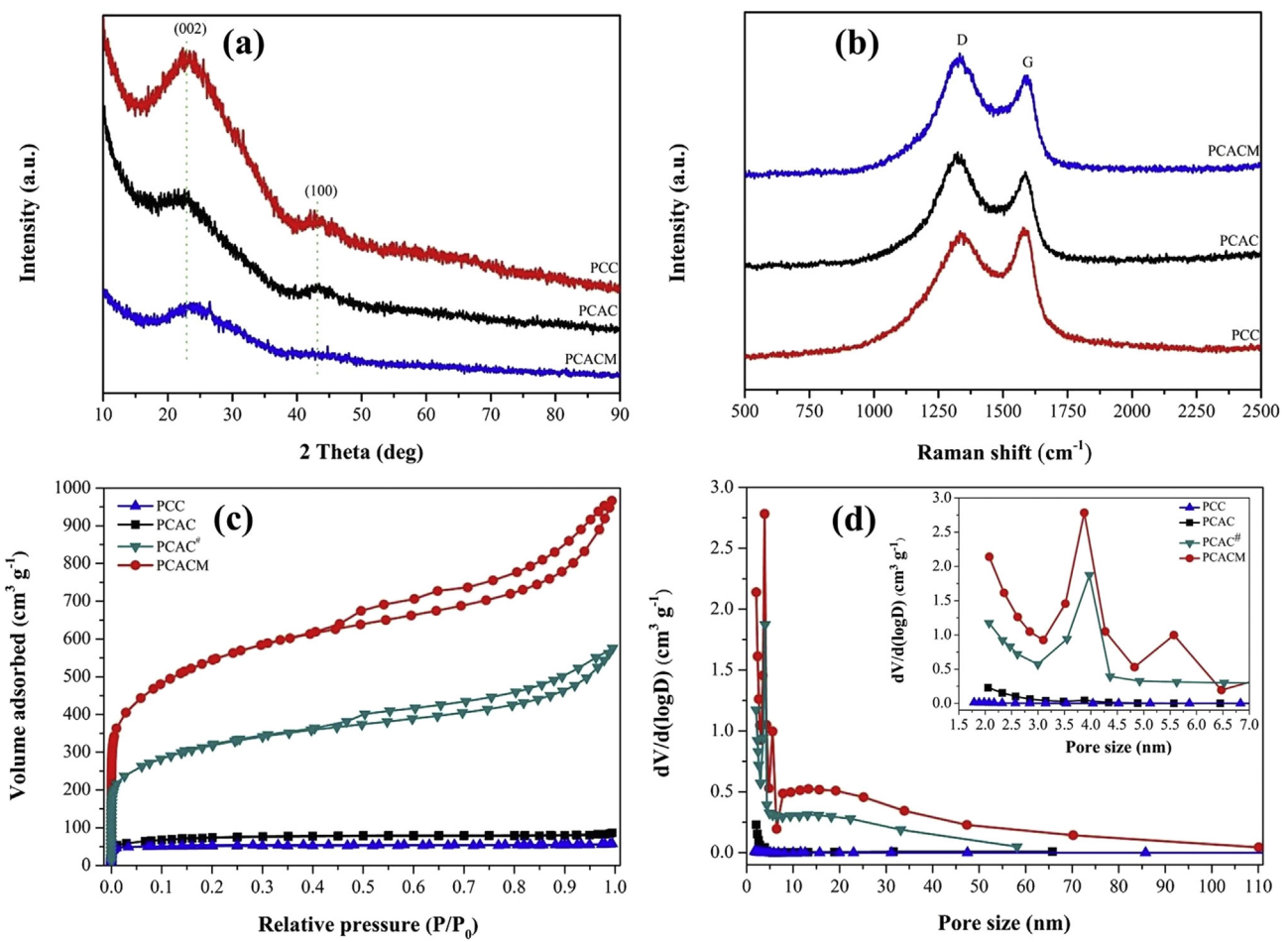


Fig. 4. STEM images of PCACM.

Fig. 5. XRD patterns (a), Raman spectra (b), N₂ adsorption-desorption isotherms (c), and pore size distributions (d) of PCC, PCAC, PCAC[#], and PCACM.

reactions shown in Eqs. (2)–(7). It is interesting that both PCAC[#] and PCACM exhibit opposite behaviors. As shown in Fig. 5c, a sharp rise at the low relative pressures ($P/P_0 < 0.05$) in their N₂ adsorption-desorption isotherms, which indicate the existence of a large number of micropores. In addition, Fig. 5c reveals apparent hysteresis loops in the range of $P/P_0 = 0.45$ –1.00, suggesting the formation of mesopores and macropores in PCAC[#] and PCACM due to the aforementioned chemical activations. Compared with the

relatively broad pore size distributions for PCAC[#] and PCACM shown in Fig. 5d, PCC has not obvious pores and PCAC only has mesopores in the range of 2.0–3.5 nm under the analytic conditions. Noticeably, PCACM demonstrates a wider pore size distribution than PCAC[#].

The chemical activation could introduce tremendous pores into the activated carbon materials and this is expected to result in large surface area and high total pore volume. As shown in Table 1, PCC

has a quite low specific surface area and total pore volume ($S_{\text{BET}} = 154.3 \text{ m}^2 \text{ g}^{-1}$, $V_p = 0.089 \text{ cm}^3 \text{ g}^{-1}$). These parameters are smaller than those of PCAC ($S_{\text{BET}} = 264.9 \text{ m}^2 \text{ g}^{-1}$, $V_p = 0.134 \text{ cm}^3 \text{ g}^{-1}$) and PCAC[#] ($S_{\text{BET}} = 1113.1 \text{ m}^2 \text{ g}^{-1}$, $V_p = 0.890 \text{ cm}^3 \text{ g}^{-1}$). As for PCACM, the values of S_{BET} and V_p are as high as $1893.0 \text{ m}^2 \text{ g}^{-1}$ and $1.495 \text{ cm}^3 \text{ g}^{-1}$, respectively. The hierarchical porous texture and high surface area are especially favorable for energy storage of EDLC.

XPS analysis is performed to determine the surface composition of the resulting materials. As shown in Fig. 6a, the XPS survey scans show three key elements, i.e., C, O, and N. As shown in Table 2, the content of nitrogen in the PCC is 2.73%, which is higher than that in PCAC (1.43%) and PCACM (1.04%). Similar phenomenon could be found for the percentage of oxygen, which is decreased from 23.05% in PCC to 13.08% in PCAC and 13.15% in PCACM. This is due to the poor thermal stability of the nitrogen and oxygen species at high temperatures. The N 1s spectra shown in Fig. 6b can be deconvoluted to two peaks corresponding to two types of nitrogen functional group, namely pyridinic N (398.2–398.5 eV), in which N is bonded to two C atoms in six-membered rings at the edge of the graphene layer, and pyrrolic N and/or pyridonic N (400.1–400.3 eV), in which N is associated with phenolic or carbonyl group on the neighbor carbon atoms of the five-membered ring [2]. The lone pair electrons in pyridinic-N group could improve the wetting nature of electrode and the graphitic-N could improve the charge density of carbon network, thus resulting better electron conductivity. In addition, both N-pyridinic and N-pyrrolic functionalities may promote the electron transfer between electrode and electrolyte [58–60]. The O 1s spectra depicted in Fig. 6c are deconvoluted into two peaks located at 532.0–532.2 eV and 533.8–534.4 eV, corresponding to C=O and O=C=O groups, respectively. These functionalities also play an important role in improving wettability of the material surface and are considered to contribute to pseudocapacitance [61].

3.2. Electrochemical performance

The electrochemical properties of PCC, PCAC, PCAC[#], and PCACM are characterized in an alkaline medium (6.0 M KOH) by means of a three-electrode system. In order to further investigate the electrochemical cell performance, a symmetric supercapacitor is also assembled by employing two same PCACM electrodes in 1.0 M Na₂SO₄ aqueous electrolyte. Both the solutions are the generally used electrolytes for supercapacitor.

3.2.1. Electrochemical performance in the three-electrode system

Fig. 7a shows the CV curves of PCC, PCAC, PCAC[#], and PCACM at a scan rate of 50 mV s⁻¹ in the three-electrode system. The CV curves

Table 1

Textural and structural characteristics of the resulting materials.

Material	$S_{\text{BET}}^{\text{a}}$ ($\text{m}^2 \text{ g}^{-1}$)	S_M^{b} ($\text{m}^2 \text{ g}^{-1}$)	S_{Ex}^{c} ($\text{m}^2 \text{ g}^{-1}$)	V_p^{d} ($\text{cm}^3 \text{ g}^{-1}$)	V_M^{e} ($\text{cm}^3 \text{ g}^{-1}$)	D_a^{f} (nm)
PCC	154.3	133.1	21.2	0.089	0.071	4.75
PCAC	264.9	145.0	119.9	0.134	0.061	3.20
PCAC [#]	1113.1	372.5	740.6	0.890	0.167	4.66
PCACM	1893.0	642.4	1250.6	1.495	0.289	4.53

^a S_{BET} , specific surface area calculated by the BET method.

^b S_M , micropore area calculated by the V-t method (t-plot method micropore analysis).

^c S_{Ex} , external surface area calculated by the V-t method (t-plot method micropore analysis).

^d V_p , total pore volume determined by N₂ adsorption at a relative pressure of 0.99.

^e V_M , micropore volume calculated by the V-t method (t-plot method micropore analysis).

^f D_a , mean pore diameter obtained from the desorption isotherm by the BJH method.

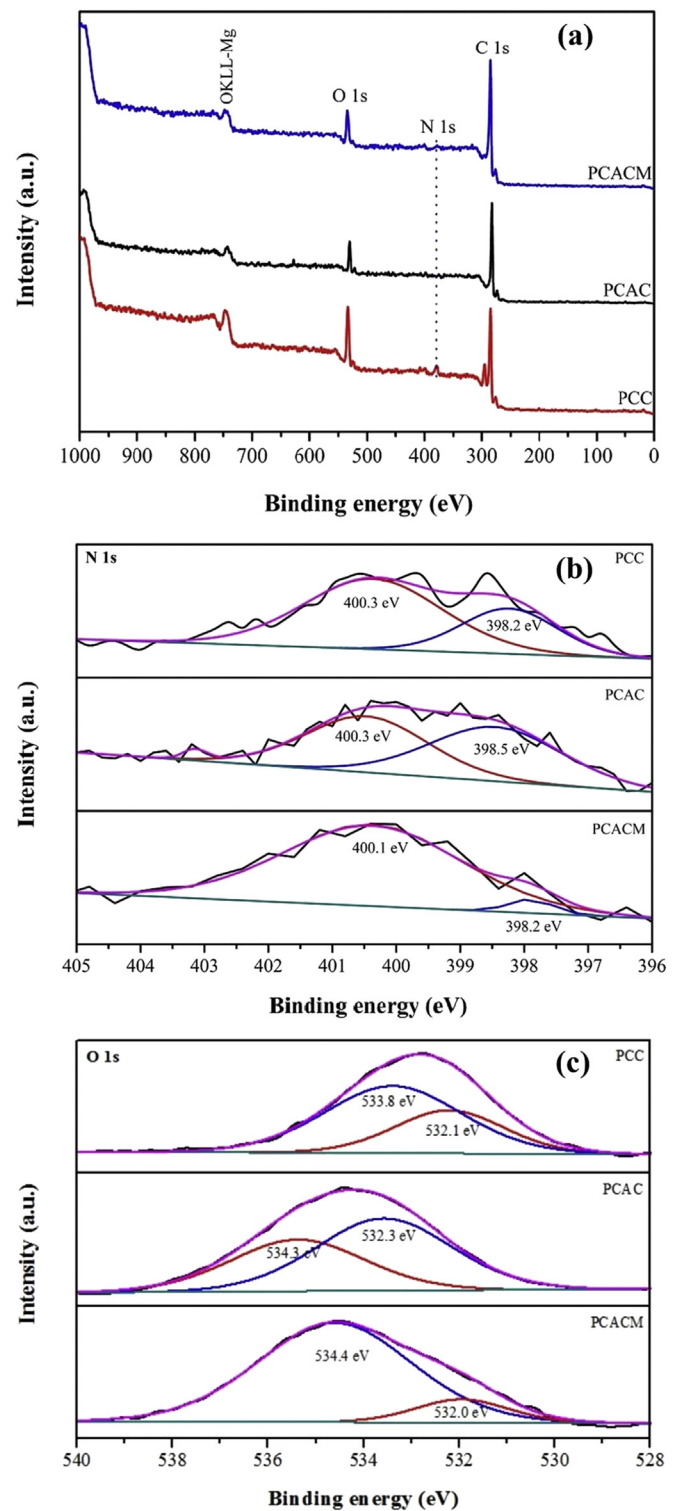


Fig. 6. XPS survey spectra (a), high-resolution N 1s spectra (b), and high-resolution O 1s spectra (c) of PCC, PCAC, and PCACM.

Table 2

Element composition of the resulting materials determined by XPS analysis.

Material	C (%)	O (%)	N (%)
PCC	74.21	23.05	2.73
PCAC	85.49	13.08	1.43
PCACM	85.81	13.15	1.04

successively present a rectangular-like shape with obvious hump at low potential region, and the hump becomes progressively less obvious. This is also an indicative of the combination effects of EDLC and pseudo-capacitance (oxidation or reduction reaction) result from the active nitrogen and/or oxygen heteroatoms [55,56]. Moreover, the area surrounded by CV curves for PCACM electrode is apparently larger than that of the PCC, PCAC[#], and PCAC electrode at the same scan rate, implying the higher specific capacitance of PCACM electrode. The excellent capacitive behavior may result from the high specific surface area and more developed porosity,

which are advantage to fast charge transfer during the faradaic reactions. Fig. 7b gives the representative CV curves of the PCACM with various sweep rates ranging from 5 to 100 mV s⁻¹. It is clearly seen that CV curves, even at 100 mV s⁻¹, are quasi-rectangular in shape along the current-potential axis, demonstrating the excellent capacitance behavior and fast diffusion of electrolyte ions into the electrode.

The GCD curves for the resulting materials at a current density of 1.0 A g⁻¹ showed in Fig. 7c exhibit almost triangle shape, indicating high reversible behavior during charge-discharge process.

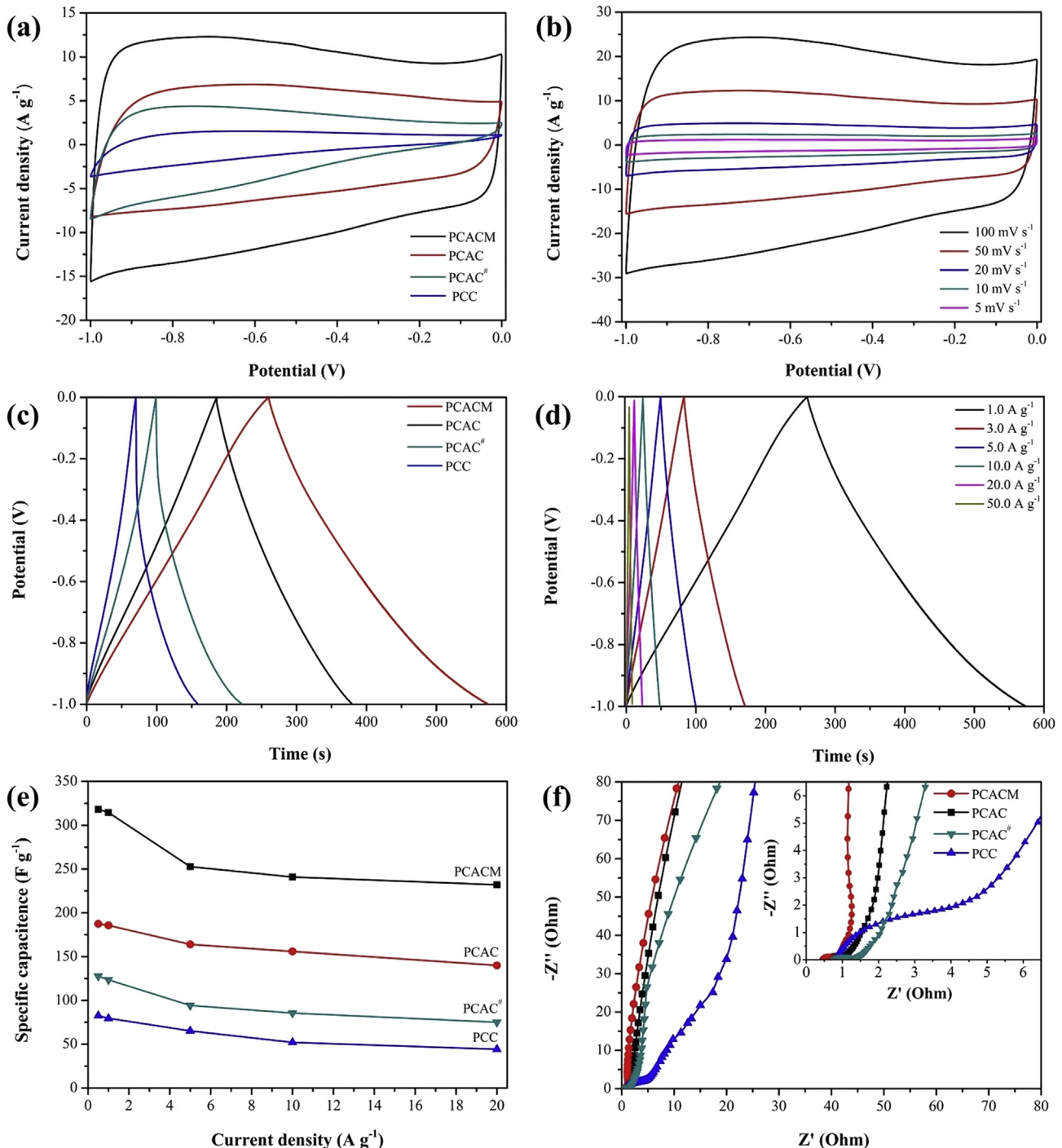


Fig. 7. Electrochemical performance of PCC, PCAC, PCAC[#], and PCACM in the three-electrode system: (a) CV curves of PCC, PCAC, PCAC[#], and PCACM at 50 mV s⁻¹; (b) CV curves of PCACM at various scan rates; (c) GCD curves of PCC, PCAC, PCAC[#], and PCACM at 1 A g⁻¹; (d) GCD curves of PCACM at different current densities; (e) specific capacitance of PCC, PCAC, PCAC[#], and PCACM at different current densities; and (f) Nyquist plots of PCC, PCAC, PCAC[#], and PCACM.

Additionally, it clearly demonstrates the capacitance increases as following: PCC < PCAC[#] < PCAC < PCACM. This might be ascribed to that PCAC and PCAC[#] possess higher porosity than PCC, which benefits facile and fast electrolyte ion transport and shortens the diffusion distances from electrolyte to the inner micro-mesopore surface. As for PCACM, it is not only activated by KOH to produce micro-mesopores, but also generated a mass of meso-macropores by the *in situ* nickel oxides nanoparticle formation and etching during thermal treatment. These result in the highest specific capacitive of PCACM. The GCD curves for PCACM at various current densities are shown in Fig. 7d. It can be seen that all curves are almost symmetrical and linear at increased current densities ranging from 1.0 to 50.0 A g⁻¹, which is a typical characteristic of the ideal capacitor with good electrochemical reversibility.

The specific capacitance of the resulting materials versus current density is summarized in Fig. 7e. Apparently, PCACM demonstrates an improved specific capacitance than the others. Its specific capacitances are as high as 318.3 and 314.6 F g⁻¹ at 0.5 and 1.0 A g⁻¹, respectively. Moreover, even at a high current rate of 20 A g⁻¹, PCACM still delivers a high capacitance of 232.0 F g⁻¹, which is about 72.9% of the initial capacitance at 0.5 A g⁻¹. Whereas, PCC exhibits only a 53.6% initial capacitance retention. Additionally, it is noteworthy that the specific capacitance of PCACM is among the highest reported for other activated carbons from various biomass precursors (Table 3). These results confirm the excellent rate capability and high capacitance retention of PCACM, which are critical for high-performance supercapacitors.

The electrochemical impedance spectroscopy (EIS) is employed in Fig. 7f. The Nyquist plots shows that the straight line in the low-frequency region represents the capacitive behavior of the electrode and the high frequency semicircle is the equivalent series resistance (ESR), which is related to the electrode conductivity and the charge-transfer resistance in the electrode materials [68]. Apparently, the interfacial contact resistance of PCACM electrode is smaller than the other electrodes, meaning that in-plan pores can effectively reduce ion diffusion resistance. Moreover, compared with the others, the PCACM electrode has lower electrode resistivity in the high frequency region.

The electrochemical difference could be explained as following: On the one hand, the high specific area is favorable for improving electrolyte contact and accumulating more electrolyte ions, and thus enhances the charge storage density; On the other hand, the presence of meso/macropores not only makes the inner micropore surface more electrochemically accessible for electrolyte ions and more charges to be accumulated in the micropores but also

facilitates the fast diffusion of electrolyte ions in the pore channels at high current densities. In addition, both the nitrogen- and oxygen-containing functional groups not only improve the hydrophilicity and wettability of the resulting carbon-based materials that results in good interfacial adhesion with electrolyte but also participates in reversible redox reaction and generates remarkable pseudocapacitance [2]. That is to say, the unique characteristics of PCACM, such as the natural tubular architecture, the nanomesh structure with hierarchical pores, high specific surface area, and the existence of nitrogen- and oxygen-containing functional groups, make it promising to be an ideal electrode candidate for supercapacitors.

3.2.2. Electrochemical performance in the two-electrode system

Fig. 8a displays the CV curves of PCACM symmetric supercapacitor operated in different voltage windows at 50 mV s⁻¹. It is clear that the loop displays a rectangular-like shape without obvious increase of cathode current in the voltage range of 1.0–1.8 V and initial rapid increase of cathode current at 2.0 V. Fig. 8b shows the CV curves of the symmetric supercapacitor in the voltage range of 0–1.8 V. The CV curves still retain the rectangular shape and do not change even at a scan rate as high as 100 mV s⁻¹, indicating the quick charge propagation capability and the facile ion transport within PCACM.

The GCD curves shown in Fig. 8c are highly linear and symmetrical at current densities of 0.2–10.0 A g⁻¹, implying its low overall resistance, excellent electrochemical reversibility and charge-discharge properties. The relationship of specific capacitance and current density is shown as Fig. 8d. It is can be seen that the PCACM supercapacitor device exhibits a satisfactory capacitance retention. The specific capacitance is calculated to be 44.29 F g⁻¹ at 0.2 A g⁻¹. Even at a high current density of 10.0 A g⁻¹, PCACM still maintains a specific capacitance of 22.51 F g⁻¹ with an initial capacitance retention of 48.63%. It is a common phenomenon that the specific capacitance decreases with the increase of current density. This is due to the increasing of IR for supercapacitor, which comes from the existence of electrical resistance and the generation of concentration polarization. As for the PCACM symmetric cell, in our own opinion, the apparently low rate capability is also may be ascribed to the wide current density range (0.2–10 A g⁻¹).

Nyquist plots are shown in Fig. 8e. The steep linear curves in the low frequency region indicate nearly ideal capacitive performance and the semi-circle in the high frequency region represents the charge transfer resistance [68,69]. PCACM possesses the steep slope of the curves and the small diameter of semicircle (0.3 Ω), meaning

Table 3
Comparison of specific capacitance, energy density, and power density of various biomass derived carbons.

Biomass	Specific capacitance ^a (C _m , F g ⁻¹)	Energy density (E, Wh kg ⁻¹)	Power density (P, W kg ⁻¹)	Ref.
Willow catkin	279 (1.0 A g ⁻¹)	—	—	[2]
Willow catkin	292 (1.0 A g ⁻¹)	37.9	700	[19]
Willow catkin	298 (0.5 A g ⁻¹)	21.0	180.0	[54]
Cotton	189.8 (1.0 A g ⁻¹)	—	—	[21]
Pomelo peel	260 (1.0 A g ⁻¹)	27.75	300	[31]
Bamboo shell	204 (1.0 A g ⁻¹)	—	—	[48]
Argan seed shell	330.2 (1.0 A g ⁻¹)	—	—	[49]
Poplar catkin	—	7.5	—	[52]
Peanut shell	—	19.3	1007	[62]
Stiff silkworm	304.0 (1.0 A g ⁻¹)	7.9	—	[63]
Lotus seedpod	402.0 (0.5 A g ⁻¹)	12.5	260.0	[64]
Oil palm leave	368 (0.06 A g ⁻¹)	13.0	41.0	[65]
Reed straw	245.2 (1.0 A g ⁻¹)	612	4460	[66]
Bagasse	320 (0.5 A g ⁻¹)	20.0	182.0	[67]
Poplar catkin	314.6 (1.0 A g ⁻¹)	20.9	180.1	our work

^a Specific capacitance is calculated from the charge-discharge profiles in the three-electrode system using the aforementioned Eq. (9).

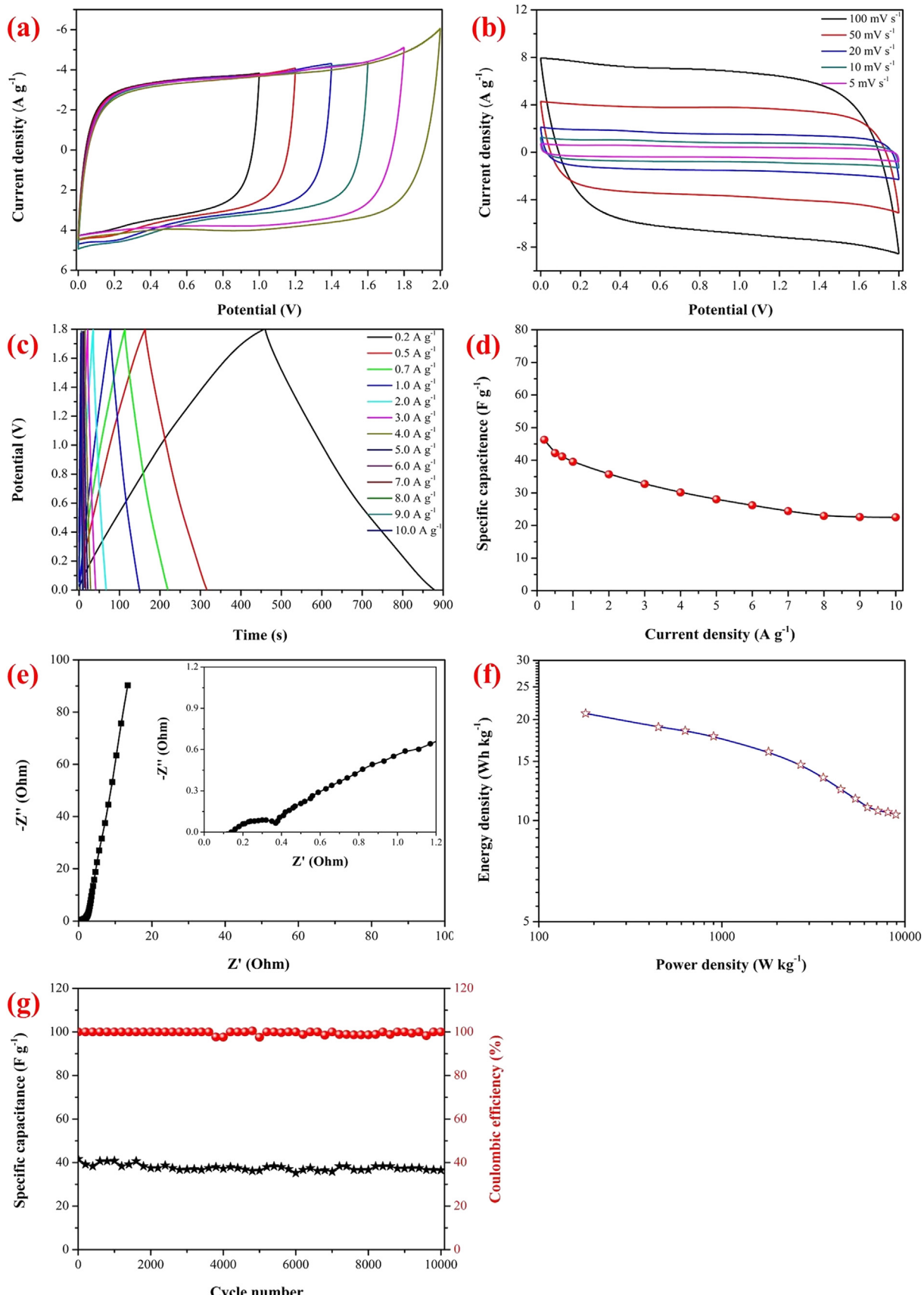


Fig. 8. Electrochemical performance of PCACM in the two-electrode system: (a) CV curves at 50 mV s^{-1} ; (b) CV curves at various scan rates; (c) GCD curves at various current densities; (d) specific capacitance at different current densities; (e) Nyquist plots; (f) Ragone plots; and (g) specific capacitance and columbic efficiency at 1.0 A g^{-1} .

that the reduced ion diffusion resistance.

Cycle stability is an important factor to estimate materials for practical applications. In Fig. 8f, PCACM-based electrode demonstrates a good electrochemical stability with 87.6% capacitance retention after 10000 cycles at 1 A g^{-1} , and the coulombic efficiency remains nearly 100%. Fig. 8g shows the Ragone plots of average specific energy versus average specific power. The specific energy density of the device is about 20.86 Wh kg^{-1} at a power density of 180.13 W kg^{-1} , which is comparable or even much higher than those of other activated carbons reported in literature (Table 3). Furthermore, the assembled asymmetric cell displays a good power characteristic, and it keeps an acceptable energy density of 10.42 Wh kg^{-1} when the power density reaches up to $8928.63 \text{ W kg}^{-1}$.

4. Conclusions

In summary, we demonstrated an efficient method to successfully prepare the hollow activated carbon nanomesh (PCACM) from poplar catkins. The results showed that PCACM kept the natural tubular morphology of poplar catkins with a fascinating nanomesh structure on the walls. Meanwhile, it exhibited much large specific surface area ($S_{\text{BET}} = 1893.0 \text{ m}^2 \text{ g}^{-1}$) and high pore volume ($V_p = 1.495 \text{ cm}^3 \text{ g}^{-1}$). As supercapacitor electrode, its specific capacitance is as high as 314.6 F g^{-1} at 1.0 A g^{-1} in a three-electrode system. The symmetric supercapacitor based on PCACM displayed a high energy density of 20.86 Wh kg^{-1} at a power density of 180.13 W kg^{-1} within a wide voltage rage of $0\text{--}1.8 \text{ V}$. In addition, the PCACM materials also exhibit superior cycling stability and coulombic efficiency. Therefore, PCACM is expected to be a promising candidate as advanced electrodes for future supercapacitor and full cells.

Acknowledgements

Financial supports from the National Natural Science Foundation of China (Nos. U1304203, U1404503 and 21403053), the Natural Science Foundation of Henan Province (No. 162300410258), the Foundation of Henan Educational Committee (No. 16A150046), and the Innovation Foundation of Zhengzhou University (Nos. 201610459062 and 2016xjxm251) are greatly acknowledged.

Appendix A. Supplementary data

Supplementary data related to this article can be found at <http://dx.doi.org/10.1016/j.jpowsour.2017.07.021>.

References

- [1] D.W. Wang, Y.G. Min, Y.H. Yu, B. Peng, A general approach for fabrication of nitrogen-doped graphene sheets and its application in supercapacitors, *J. Colloid. Interf. Sci.* 417 (2014) 270–277.
- [2] K. Wang, N. Zhao, S.W. Lei, R. Yan, X.D. Tian, J.Z. Wang, Y. Song, D.F. Xu, Q.G. Guo, L. Liu, Promising biomass-based activated carbons derived from willow catkins for high performance supercapacitors, *Electrochim. Acta* 166 (2015) 1–11.
- [3] C.D. Lokhande, D.P. Dubal, O.S. Joo, Metal oxide thin film based supercapacitors, *Curr. Appl. Phys.* 11 (2011) 255–270.
- [4] A.G. Pandolfo, A.F. Hollenkamp, Carbon properties and their role in supercapacitors, *J. Power Sources* 157 (2006) 11–27.
- [5] P. Zhou, L.Q. Fan, J.H. Wu, C. Gong, J.F. Zhang, Y.G. Tu, Facile hydrothermal synthesis of NiTe and its application as positive electrode material for asymmetric supercapacitor, *J. Alloy Compd.* 685 (2016) 384–390.
- [6] X.Y. Zhao, X.L. Li, Y.J. Zhao, Z.L. Su, Y.Y. Zhang, R.H. Wang, Facile synthesis of Tremelliflor Co_{0.85}Se nanosheets for supercapacitor, *J. Alloy Compd.* 697 (2017) 124–131.
- [7] H. Lee, S. Hong, J. Lee, Y.D. Suh, J. Kwon, H. Moon, H. Kim, J. Yeo, S.H. Ko, Highly stretchable and transparent supercapacitor by Ag-Au core-shell nanowire network with high electrochemical stability, *ACS Appl. Mater. Inter* 8 (2016) 15449–15458.
- [8] M.S. Zhu, Y. Huang, Q.H. Deng, J. Zhou, Z.X. Pei, Q. Xue, Y. Huang, Z.F. Wang, H.F. Li, Q. Huang, C.Y. Zhi, Highly flexible freestanding supercapacitor electrode with enhanced performance obtained by hybridizing polypyrrole chains with MXene, *Adv. Energy Mater* 6 (2016) No. 1600969.
- [9] Y.X. Zeng, M.H. Yu, Y. Meng, P.P. Fang, X.H. Lu, Y.X. Tong, Iron-based supercapacitor electrodes: advances and challenges, *Adv. Energy Mater* 6 (2016) No. 1601053.
- [10] L.H. Liu, Y. Luo, W.F. Tan, Y.S. Zhang, F. Liu, G.H. Qiu, Facile synthesis of birnessite-type manganese oxide nanoparticles as supercapacitor electrode materials, *J. Colloid. Interf. Sci.* 482 (2016) 183–192.
- [11] B. Ameri, S.H. Davarani, R. Roshani, H.R. Moazami, A. Tadjarodi, A flexible mechanochemical route for the synthesis of copper oxide nanorods/nanoparticles/nanowires for supercapacitor applications: the effect of morphology on the charge storage ability, *J. Alloy Compd.* 695 (2017) 114–123.
- [12] X.H. Wang, H.Y. Xia, X.Q. Wang, J. Gao, B. Shi, Y. Fang, Facile synthesis ultrathin mesoporous Co₃O₄ nanosheets for high-energy asymmetric supercapacitor, *J. Alloy Compd.* 686 (2016) 969–975.
- [13] G. Meng, Q. Yang, X.C. Wu, P.B. Wan, Y.P. Li, X.D. Lei, X.M. Sun, J.F. Liu, Hierarchical mesoporous NiO nanoarrays with ultrahigh capacitance for aqueous hybrid supercapacitor, *Nano Energy* 30 (2016) 831–839.
- [14] Q.Q. Hu, Z.X. Gu, X.T. Zheng, X.J. Zhang, Three-dimensional Co₃O₄@NiO hierarchical nanowire arrays for solid-state symmetric supercapacitor with enhanced electrochemical performances, *Chem. Eng. J.* 304 (2016) 223–231.
- [15] S. Jia, Y.Y. Ma, H. Wang, J.L. Key, D.J.L. Brett, R.F. Wang, Cage-like Mn₂O₃-Mn₂O₃ hollow spheres with high specific capacitance and high rate capability as supercapacitor material, *Electrochim. Acta* 219 (2016) 540–546.
- [16] N. Goubard-Bretesche, O. Crosnier, G. Buvat, F. Favier, T. Brousse, Electrochemical study of aqueous asymmetric FeWO₄/MnO₂ supercapacitor, *J. Power Sources* 326 (2016) 695–701.
- [17] N. Choudhary, C. Li, H.S. Chung, J. Moore, J. Thomas, Y. Jung, High-performance one-body core/shell nanowire supercapacitor enabled by conformal growth of capacitive 2D WS₂ layers, *ACS Nano* 10 (2016) 10726–10735.
- [18] B. Guan, Y. Li, B.Y. Yin, K.F. Liu, D.W. Wang, H.H. Zhang, C.J. Cheng, Synthesis of hierarchical NiS microflowers for high performance asymmetric supercapacitor, *Chem. Eng. J.* 308 (2017) 1165–1173.
- [19] L.J. Xie, G.H. Sun, F.Y. Su, X.Q. Guo, Q.Q. Kong, X.M. Li, X.H. Huang, L. Wan, W. Song, K.X. Li, C.X. Lv, C.M. Chen, Hierarchical porous carbon microtubes derived from willow catkins for supercapacitor applications, *J. Mater. Chem. A* 4 (2016) 1637–1646.
- [20] D.K. Singh, K.S. Krishna, S. Harish, S. Sampath, M. Eswaramoorthy, No more HF: teflon-assisted ultrafast removal of silica to generate high-surface-area mesostructured carbon for enhanced CO₂ capture and supercapacitor performance, *Angew. Chem. Int. Ed.* 55 (2016) 2032–2036.
- [21] Y. Liu, Z.J. Shi, Y.F. Gao, W.D. An, Z.Z. Cao, J.R. Liu, Biomass-swelling assisted synthesis of hierarchical porous carbon fibers for supercapacitor electrodes, *ACS Appl. Mater. Inter* 8 (2016) 28283–28290.
- [22] R.R. Salunkhe, Y.V. Kaneti, J. Kim, J.H. Kim, Y. Yamauchi, Nanoarchitectures for metal-organic framework-derived nanoporous carbons toward supercapacitor applications, *Accounts Chem. Res.* 49 (2016) 2796–2806.
- [23] D.W. Wang, G.L. Fang, T. Xue, J.F. Ma, G.H. Geng, A melt route for the synthesis of activated carbon derived from carton box for high performance symmetric supercapacitor applications, *J. Power Sources* 307 (2016) 401–409.
- [24] Z.S. Li, X.H. Hu, D.Q. Xiong, B.L. Li, H.Q. Wang, Q.Y. Li, Facile synthesis of bicontinuous microporous/mesoporous carbon foam with ultrahigh specific surface area for supercapacitor application, *Electrochim. Acta* 219 (2016) 339–349.
- [25] C. Ma, J. Sheng, C.L. Ma, R.R. Wang, J.Q. Liu, Z.Y. Xie, J.L. Shi, High-performance supercapacitor based mesoporous carbon nanofibers with oriented mesopores parallel to axial direction, *Chem. Eng. J.* 304 (2016) 587–593.
- [26] J.R. Magana, Y.V. Kolen'ko, F.L. Deepak, C. Solans, R.G. Shrestha, J.P. Hill, K. Ariga, L.K. Shrestha, C. Rodriguez-Abreu, From chromonic self-assembly to hollow carbon nanofibers: efficient materials in supercapacitor and vapor-sensing applications, *ACS Appl. Mater. Inter* 8 (2016) 31231–31238.
- [27] R.R. Rajagopal, L.S. Aravinda, R. Rajarao, B.R. Bhat, V. Sahajwalla, Activated carbon derived from non-metallic printed circuit board waste for supercapacitor application, *Electrochim. Acta* 211 (2016) 488–498.
- [28] C. Ramirez-Castro, C. Schutter, S. Passerini, A. Balducci, Microporous carbonaceous materials prepared from biowaste for supercapacitor application, *Electrochim. Acta* 206 (2016) 452–457.
- [29] J. Cai, H.T. Niu, H.X. Wang, H. Shao, J. Fang, J.R. He, H.G. Xiong, C.J. Ma, T. Lin, High-performance supercapacitor electrode from cellulose-derived, interbonded carbon nanofibers, *J. Power Sources* 324 (2016) 302–308.
- [30] L. Liu, S.D. Xu, Q. Yu, F.Y. Wang, H.L. Zhu, R.L. Zhang, X. Liu, Nitrogen-doped hollow carbon spheres with a wrinkled surface: their one-pot carbonization synthesis and supercapacitor properties, *Chem. Commun.* 52 (2016) 11693–11696.
- [31] G. Qu, S.F. Jia, H. Wang, F. Cao, L. Li, C. Qing, D.M. Sun, B.X. Wang, Y.W. Tang, J.B. Wang, Asymmetric supercapacitor based on porous N-doped carbon derived from pomelo peel and NiO arrays, *ACS Appl. Mater. Inter* 8 (2016) 20822–20830.
- [32] F. Sun, J.H. Gao, X.X. Pi, L.J. Wang, Y.Q. Yang, Z.B. Qu, S.H. Wu, High performance aqueous supercapacitor based on highly nitrogen doped carbon nanospheres with unimodal mesoporosity, *J. Power Sources* 337 (2017) 189–196.
- [33] W.Q. Tian, Q.M. Gao, L.M. Zhang, C.X. Yang, Z.Y. Li, Y.L. Tan, W.W. Qian,

- H. Zhang, Renewable graphene-like nitrogen-doped carbon nanosheets as supercapacitor electrodes with integrated high energy-power properties, *J. Mater. Chem. A* 4 (2016) 8690–8699.
- [34] C.S. Wang, T.Z. Liu, Nori-based N, O, S, Cl co-doped carbon materials by chemical activation of ZnCl₂ for supercapacitor, *J. Alloy Compd.* 696 (2017) 42–50.
- [35] Z. Bingna, X. Zhen, G. Chao, Mass production of graphene nanoscrolls and their application in high rate performance supercapacitor, *Nanoscale* 8 (2016) 1413–1420.
- [36] D.F. Yang, C. Bock, Laser reduced graphene for supercapacitor applications, *J. Power Sources* 337 (2017) 73–81.
- [37] C.M. Yin, C.A. Tao, F.L. Cai, C.C. Song, H. Gong, J.F. Wang, Effects of activation temperature on the deoxygenation, specific surface area and supercapacitor performance of graphene, *Carbon* 109 (2016) 558–565.
- [38] T.F. Qin, Z.Y. Wan, Z.L. Wang, Y.X. Wen, M.T. Liu, S.L. Peng, D.Y. He, J. Hou, F. Huang, G.Z. Cao, 3D flexible O/N co-doped graphene foams for supercapacitor electrodes with high volumetric and areal capacitances, *J. Power Sources* 336 (2016) 455–464.
- [39] Y. Zhang, G.W. Wen, P. Gao, S.F. Bi, X.F. Tang, D. Wang, High-performance supercapacitor of macroscopic graphene hydrogels by partial reduction and nitrogen doping of graphene oxide, *Electrochim. Acta* 221 (2016) 167–176.
- [40] D. Ji, H. Zhou, J. Zhang, Y.Y. Dan, H.X. Yang, A.H. Yuan, Facile synthesis of a metal-organic framework-derived Mn₂O₃ nanowire coated three-dimensional graphene network for high-performance free-standing supercapacitor electrodes, *J. Mater. Chem. A* 4 (2016) 8283–8290.
- [41] C. Choi, H.J. Sim, G.M. Spinks, X. Lepro, R.H. Baughman, S.J. Kim, Elastomeric and dynamic MnO₂/CNT core-shell structure coiled yarn supercapacitor, *Adv. Energy Mater.* 6 (2016). No. 1502119.
- [42] Y.C. Liu, X.F. Miao, J.H. Fang, X.X. Zhang, S.J. Chen, W. Li, W.D. Feng, Y.Q. Chen, W. Wang, Y.N. Zhang, Layered-MnO₂ nanosheet grown on nitrogen-doped graphene template as a composite cathode for flexible solid-state asymmetric supercapacitor, *ACS Appl. Mater. Inter* 8 (2016) 5251–5260.
- [43] P.S. Luan, N. Zhang, W.Y. Zhou, Z.Q. Niu, Q. Zhang, L. Cai, X. Zhang, F. Yang, Q.X. Fan, W.B. Zhou, Z.J. Xiao, X.G. Gu, H.L. Chen, K.W. Li, S.Q. Xiao, Y.C. Wang, H.P. Liu, S.S. Xie, Epidermal supercapacitor with high performance, *Adv. Funct. Mater.* 26 (2016) 8178–8184.
- [44] J.F. Sun, Y. Huang, C.X. Fu, Z.Y. Wang, Y. Huang, M.S. Zhu, C.Y. Zhi, H. Hu, High-performance stretchable yarn supercapacitor based on PPy@CNTs@urethane elastic fiber core spun yarn, *Nano Energy* 27 (2016) 230–237.
- [45] L.N. Ma, R. Liu, H.J. Niu, L.X. Xing, L. Liu, Y.D. Huang, Flexible and freestanding supercapacitor electrodes based on nitrogen-doped carbon networks/graphene/bacterial cellulose with ultrahigh areal capacitance, *ACS Appl. Mater. Inter* 8 (2016) 33608–33618.
- [46] L. Chen, T. Ji, L.W. Mu, J.H. Zhu, Cotton fabric derived hierarchically porous carbon and nitrogen doping for sustainable capacitor electrode, *Carbon* 111 (2017) 839–848.
- [47] D. Lei, K.H. Song, X.D. Li, H.Y. Kim, B.S. Kim, Nanostructured polyaniline/kenaf-derived 3D porous carbon materials with high cycle stability for supercapacitor electrodes, *J. Mater. Sci.* 52 (2017) 2158–2168.
- [48] B.H. Lu, L.Y. Hu, H.Y. Yin, X.H. Mao, W. Xiao, D.H. Wang, Preparation and application of capacitive carbon from bamboo shells by one step molten carbonates carbonization, *Int. J. Hydrogen Energ.* 41 (2016) 18713–18720.
- [49] A. Elmouwahidi, Z. Zapata-Benabite, F. Carrasco-Marín, C. Moreno-Castilla, Activated carbons from KOH-activation of argan (*Argania spinosa*) seed shells as supercapacitor electrodes, *Bioresour. Technol.* 111 (2012) 185–190.
- [50] L.X. Li, T. Hu, H.X. Sun, J.P. Zhang, A.Q. Wang, Pressure-sensitive and conductive carbon aerogels from poplars catkins for selective oil absorption and oil/water separation, *ACS Appl. Mater. Inter* (2017), <http://dx.doi.org/10.1021/acsami.7b04687>.
- [51] Y.G. Zhang, Y. Zhao, A. Konarov, Z. Li, P. Chen, Effect of mesoporous carbon microtube prepared by carbonizing the poplar catkin on sulfur cathode performance in Li/S batteries, *J. Alloy Compd.* 619 (2015) 298–302.
- [52] Y. Wei, Activated carbon microtubes prepared from plant biomass (poplar catkins) and their application for supercapacitors, *Chem. Lett.* 43 (2014) 216–218.
- [53] C. Chen, D.F. Yu, G.Y. Zhao, B.S. Du, W. Tang, L. Sun, Y. Sun, F. Besenbacher, M. Yu, Three-dimensional scaffolding framework of porous carbon nanosheets derived from plant wastes for high-performance supercapacitors, *Nano Energy* 27 (2016) 377–389.
- [54] Y.J. Li, G.L. Wang, T. Wei, Z.J. Fan, P. Yan, Nitrogen and sulfur co-doped porous carbon nanosheets derived from willow catkin for supercapacitors, *Nano Energy* 19 (2016) 165–175.
- [55] X.J. Wei, S.G. Wan, S.Y. Gao, Self-assembly-template engineering nitrogen-doped carbon aerogels for high-rate supercapacitors, *Nano Energy* 28 (2016) 206–215.
- [56] P. Ramakrishnan, S. Shanmugam, Electrochemical performance of carbon nanorods with embedded cobalt metal nanoparticles as an electrode material for electrochemical capacitors, *Electrochim. Acta* 125 (2014) 232–240.
- [57] G.F. Ma, Z.G. Zhang, H. Peng, K.J. Sun, F.T. Ran, Z.Q. Lei, Facile preparation of nitrogen-doped porous carbon for high performance symmetric supercapacitor, *J. Solid State Electrochem* 20 (2016) 1613–1623.
- [58] P. Ramakrishnan, S. Shanmugam, Nitrogen-doped carbon nanofoam derived from amino acid chelate complex for supercapacitor applications, *J. Power Sources* 316 (2016) 60–71.
- [59] M. Prabu, P. Ramakrishnan, P. Ganesan, A. Manthiram, S. Shanmugam, LaT_{1-0.65}Fe_{0.35}O_{3-δ} nanoparticle-decorated nitrogen-doped carbon nanorods as an advanced hierarchical air electrode for rechargeable metal-air batteries, *Nano Energy* 15 (2015) 92–103.
- [60] P. Ramakrishnan, S. Shanmugam, Nitrogen-doped porous multi-nano-channel nanocarbons for use in high-performance supercapacitor applications, *ACS Sustain. Chem. Eng.* 4 (2016) 2439–2448.
- [61] J.K. Meng, L. Fu, Y.S. Liu, G.P. Zheng, X.C. Zheng, X.X. Guan, J.M. Zhang, Gas-liquid interfacial assembly and electrochemical properties of 3D highly dispersed alpha-Fe₂O₃@graphene aerogel composites with a hierarchical structure for applications in anodes of lithium ion batteries, *Electrochim. Acta* 224 (2017) 40–48.
- [62] X.J. He, P.H. Ling, J.S. Qiu, M.X. Yu, X.Y. Zhang, C. Yu, M.D. Zheng, Efficient preparation of biomass-based mesoporous carbons for supercapacitors with both high energy density and high power density, *J. Power Sources* 240 (2013) 109–113.
- [63] C.C. Gong, X.Z. Wang, D.H. Ma, H.F. Chen, S.S. Zhang, Z.X. Liao, Microporous carbon from a biological waste-stiff silkworm for capacitive energy storage, *Electrochim. Acta* 220 (2016) 331–339.
- [64] B. Liu, X.H. Zhou, H.B. Chen, Y.J. Liu, H.M. Li, Promising porous carbons derived from lotus seedpods with outstanding supercapacitance performance, *Electrochim. Acta* 208 (2016) 55–63.
- [65] G.A.M. Ali, S.A.A. Manaf, A. Divyashree, K.F. Chong, G. Hegde, Superior supercapacitive performance in porous nanocarbons, *J. Energy Chem.* 25 (2016) 734–739.
- [66] Q.X. Xie, A.R. Zheng, S.B. Zhai, S.H. Wu, C. Xie, Y.F. Zhang, Y.F. Guan, Reed straw derived active carbon/graphene hybrids as sustainable high-performance electrodes for advanced supercapacitors, *J. Solid State Electrochem* 20 (2016) 449–457.
- [67] H.B. Feng, H. Hu, H.W. Dong, Y. Xiao, Y.J. Cai, B.F. Lei, Y.L. Liu, M.T. Zheng, Hierarchical structured carbon derived from bagasse wastes: a simple and efficient synthesis route and its improved electrochemical properties for high-performance supercapacitors, *J. Power Sources* 302 (2016) 164–173.
- [68] Y.Q. Liao, Y.L. Huang, D. Shu, Y.Y. Zhong, J.N. Hao, C. He, J. Zhong, X.N. Song, Three-dimensional nitrogen-doped graphene hydrogels prepared via hydrothermal synthesis as high-performance supercapacitor materials, *Electrochim. Acta* 194 (2016) 136–142.
- [69] Y.J. Li, N. Yu, P. Yan, Y.G. Li, X.M. Zhou, S.L. Chen, G.L. Wang, T. Wei, Z.J. Fan, Fabrication of manganese dioxide nanoplates anchoring on biomass-derived cross-linked carbon nanosheets for high-performance asymmetric supercapacitors, *J. Power Sources* 300 (2015) 309–317.